High-Aspect-Ratio GaN p – i – n Nanowires for Linear UV Photodetectors

Bruno César da Silva, Adam Biegański, Christophe Durand, Zahra Sadre Momtaz, Anjali Harikumar, David Cooper, Eva Monroy, Martien Ilse den Hertog

High Aspect Ratio GaN p-i-n Nanowires for Linear UV Photodetectors

Bruno César da Silva[1]*, Adam Biegański[2], Christophe Durand[2], Zahra Sadre Momtaz[1], Anjali Harikumar[2], David Cooper[3], Eva Monroy[2] and Martien Ilse den Hertog[1*]

[1] *University Grenoble Alpes, CNRS-Institut Néel, Grenoble F-38000, France*
[2] *University Grenoble Alpes, CEA, Grenoble INP, IRIG, PHELIQS, Grenoble F-38000, France*
[3] *University Grenoble Alpes, CEA-LETI, Grenoble F-38000, France*

ABSTRACT: Ultraviolet GaN photodetectors based on nanowires (NWs) fabricated by top-down strategies promise improved uniformity, morphology and doping control with respect to bottom-up ones. However, exploiting the advantages of the NW geometry requires sub-wavelength NW diameters. We present fabrication of large area sub-200-nm diameter top-down GaN *p-i-n* NW ultraviolet photodetectors with length over 2 µm produced from a planar specimen using nanosphere lithography followed by a combination of dry and crystallographic-selective wet etching. Photocurrent measurements in single NW devices under bias show a linear response as a function of the optical power, with increased current levels under reverse bias. The linearity proves that the drift of photogenerated carriers at the junction is the dominating photodetection mechanism, with negligible contributions from surface effects. These results demonstrate that the unique properties of NW-based photodetectors can be assessed through a scalable and low-cost fabrication process.

KEYWORDS: Gallium Nitride nanowires, top-down fabrication, nanosphere lithography, ultraviolet photodetectors, linear photoresponse

1 Introduction

The detection of ultraviolet (UV) radiation, covering the wavelength range from 10 to 400 nm, finds many uses, from military to space applications[1–4]. Restrictive specifications like low noise and high robustness to cosmic radiation exclude many conventional materials. Gallium Nitride (GaN) is a strong candidate to cover all the requirements, since it has a direct energy bandgap of 3.4 eV at room temperature, allowing the fabrication of devices with efficient absorption of UV radiation and making it solar blind at the same time, with *p-n* junction devices having excellent performance in terms of dark noise and speed[5–8]. The ongoing miniaturization of optoelectronic devices allows advantages like cost reduction, improved integration and reduced capacitance, which has motivated research in nanowire (NW) devices[9–12]. GaN NW UV photodetectors are interesting since they can present low dark current and excellent spectral selectivity, but their photoresponse usually scales sub-linearly with the optical power due to surface effects[13,14]. Linearity can be obtained in the case of reverse-biased very thin, entirely depleted NWs[15], or in reverse-biased p-n junctions[14].

Vertically aligned GaN NWs on a conductive substrate can be obtained by bottom-up methods (metal-seeded/catalyst-free growth or selective area growth) or by top-down fabrication from planar layers. The bottom-up synthesis of NWs offers lower density of extended defects[16] and the possibility to combine materials with different lattice parameter thanks to the elastic surface relaxation of the wires[17,18]. However, it suffers from issues like non-uniform doping[19], defects due to the NW coalescence[20,21], and morphological inhomogeneities[22,23]. On the other hand, top-down nanowires produced through etching processes[24,25] present improved doping control and higher uniformity, but the reduction in diameter may present limitations related to the crystalline defects induced during the etching

process[26].

The fabrication of nanometer-scale patterns in top-down approaches can be achieved using various techniques such as electron beam lithography (EBL), nano-imprint and deep UV lithography. However, it is worth noting that the former is known for being expensive, due to the needy to use dedicated patterning equipment, and EBL can be time-consuming (i.e., not scalable). In contrast, alongside nano-imprint, nanosphere lithography offers an approach that allows large-area fabrication (scalable) and at a relatively low cost. Nanosphere lithography is a route that has been used to produce large area top-down GaN NWs[27–33]. Long NWs require large nanospheres, in order to have a mask that withstands the long dry etching process. However, this imposes a limitation to reduce the nanowire diameter. Long nanowires with high aspect ratio are required for flexible electronics[34] or energy conversion devices[35], for instance. Diameter and aspect ratio are also important in nanowire photonic devices: To exploit the advantages of the nanowire geometry, the diameter of the objects must be shorter than the wavelength of the interacting photons[36,37], and the nanowire diameter is critical to obtain linear devices[15,38].

In the last years, different authors[30,32] have shown the fabrication of GaN LEDs decoupling the NW pattern formation (defined by polystyrene nanospheres) and the nanowire length, by using a metal layer as hard mask for the dry/wet etching steps. However, the resulting nanowires were either relatively thick (diameter > 400 nm) or had limited aspect ratio (length/diameter < 17).

In this work, we have used a similar approach to demonstrate the fabrication of top-down UV photodetectors based on single GaN *p-i-n* junction nanowires, using Cl_2-BCl_3 dry etching and KOH-based wet etching. We show that the combination of polystyrene nanospheres and a SiO_2 layer as hard mask allows the independent control over the nanowire length and pitch of the nanowire array and can produce large area thin nanowires with aspect ratio higher than 30. Current-voltage (I-V), differential phase contrast (DPC) with a segmented detector in scanning transmission electron microscopy (STEM) and electron beam induced current (EBIC) measurements confirm the presence of the built-in electric field due to the *p-i-n* junction, in a lamella sample and as-fabricated NW, respectively. The performance of a single GaN *p-i-n* junction NW is studied by photocurrent measurements: an enhancement in the photocurrent under reverse bias and a linear response with the excitation power is observed at all applied bias values between -2 and 2V. These results show that linear UV photodetectors based on GaN *p-i-n* nanowires can be achieved using a low-cost scalable process.

2 Experimental

The GaN *p-i-n* planar sample was grown on c-sapphire substrates by Metal Organic Vapor Phase Epitaxy (MOVPE), as schematically shown in Fig. 1(a), using trimethylgallium (TMGa) and ammonia (NH_3) as precursors. The sample consist of a 700-nm-thick non-intentionally-doped GaN buffer layer grown at 1050°C, followed by 1.8-µm-thick *n*-doped GaN[39], a 45-nm-thick intermediate (undoped) region, and a 1.9-µm-thick *p*-doped region [40], as indicated in Fig. 1(a). Doping was achieved by using diluted silane (SiH_4) at a growth temperature of 1050 °C for the *n*-type layer. Then, the silane flux is stopped and the temperature is reduced to 950°C in 90 s, corresponding to the growth of about 45 nm of unintentionally-doped GaN. Next, the *p*-type segment is grown using biscyclopentadienyl-magnesium ($MgCp_2$) for the Mg doping. An annealing step at 700°C for 20 min under N_2 is performed at the end of the growth process, followed by a post-growth rapid thermal annealing at 800°C for 1 min under 500 sccm of N_2 to activate the Mg-dopants. As expected for a standard planar GaN growth by MOCVD on sapphire, the sample is a Ga-polar specimen.

A 350-nm-thick lamella specimen was prepared using a FEI Strata dual-beam focused ion beam (FIB). STEM-DPC was used to confirm the presence of the built-in electric field due to the *p-i-n* junction. The DPC was performed using a four-quadrant detector in a FEI Titan Ultimate aberration-corrected (S)TEM microscope operated at 200 kV with a condenser aperture of 50 µm, semi-convergence angle of 0.18 mrad, beam current of 93 pA, camera length of 13.5 m, pixel (step) size of 4 nm and dwell time of 20 µs.

The electron beam induced current (EBIC) experiment was performed in an FEI Inspect F50 SEM. Data were acquired at 4 kV with a beam current of 20 pA. The EBIC current was collected using a Keithley 6485 picoamp meter. Current-voltage (I-V) measurements were recorded using an Agilent 4155C semiconductor parameter analyzer. Photocurrent measurements as function of optical power

were carried out using an unfocused continuous-wave HeCd laser at 325 nm. The nanowire was biased and connected to the $\times 10^6$ V/A transimpedance amplifier integrated in a Stanford Research Systems SRS830 lock-in amplifier. All measurements were carried out at room temperature.

3 Results and discussion

Fig. 1(b) shows secondary ion mass spectrometry (SIMS) profiles of the planar GaN *p-i-n* sample under study. The dopant concentration in the bulk areas is about $[\mathrm{Si}] = 4.9 \times 10^{18}\ cm^{-3}$ and $[\mathrm{Mg}] = 3.9 \times 10^{19}\ cm^{-3}$. The presence of the built-in electric field due to the *p-i-n* junction was confirmed by DPC-STEM (Fig. 2(a)) using a low magnification STEM mode[41,42], measured in a 350 nm thick lamella prepared by FIB, Fig. 2(b). In DPC, the deflection of the electron beam is measured on a four-quadrant detector. Taking the difference of incident electron intensity on opposing quadrants, the deflection of the electron beam due to the internal fields can be visualized at nm length scales. Due to the electric field, the beam is deflected towards the *n* layer (turquoise color coding in Fig. 2(a)). The sample was tilted off-axis in order to minimize the diffraction contrast. The field was clearly visible as a horizontal turquoise line parallel to the sample surface, at the expected location, i.e. 1.9 µm below the sample surface. A depletion width of (50 ± 11) nm was measured, as illustrated in Fig. 2(c), which is in good agreement with the expected width of the intermediate region. Both the SIMS and DPC experimental results allowed to validate the quality of the planar *p-i-n* junction according to the growth conditions in terms of doping concentration, presence of a built-in electric field and depletion region prior to the nanowire fabrication.

The fabrication process of top-down nanowires is adapted from the two-step crystallographic-selective etching described in ref.[43]. Taking that information as a reference, we performed tests using both silica and polystyrene spheres, and we considered several diameters (details can be found in supporting information SI1). In a first experiment, we observed that it was not possible to use silica spheres directly as masks for producing a pattern of long GaN NWs since the etching cannot penetrate deep between the NWs (see Supporting Information Fig. S1a and b). Therefore, in order to create a pattern of well-separated dots to serve as a mask for the dry etching of GaN NWs, it is important to be able to shrink the diameter of the nanospheres, to separate them Unfortunately, attempts to reduce the sphere diameter using SF_6 and O_2 led to a degradation of the spherical morphology (see Supporting Information Fig. S1c). As a result, they were unsuitable for generating a pattern of NWs. In view of these problems, we decided to use polystyrene spheres as a mask (details in Supporting Information SI2). In a first attempt, we used polystyrene spheres with a diameter of 3.2 µm, as shown in Supporting Information SI2. This choice was motivated by the ability to uniformly reduce their diameter using a RIE O_2 plasma. Well defined and separated array of GaN structures were produced (see Supporting Information Fig. S2), however, with limited aspect ratio and diameter, due to concurrent etching of the Ga-polar c-plane during the KOH-based etching process and the limited selectivity of the polystyrene as a mask for GaN dry etching, details can be found in Supporting Information SI2. Therefore, in order to achieve a well separated and defined array of high aspect (length/diameter) ratio nanowires with diameters below 200 nm, we decided to follow a process where we combine 1 µm polystyrene spheres and a 600 nm thick SiO_2 layer as mask. The shrunk polystyrene spheres are used to create the nm-scale pattern, then the pattern is transferred to the SiO_2, which is used as a hard mask for GaN dry and wet etchings.

The final process is described schematically in Figure 3, and experimental SEM images are shown of respective fabrication steps in Figure 4. The top down fabrication was carried out on 7×7 mm^2 specimens that were diced from the as-grown wafer. First, a 600 nm SiO_2 layer was deposited on top of the GaN *p-i-n* planar sample using plasma-enhanced chemical vapor deposition (PECVD). Then, polystyrene spheres with a diameter of 1 µm were drop cast on top of the SiO_2 layer. To obtain a monolayer coverage of the sample, we prepared a dilution of 1% weight in water so that the good amount of spheres is contained in a 50 µl droplet. The droplet was applied on the sample with a micropipette, and dried at an angle of 10° (with respect to the horizontal plane)[44]. The result was the single-layer compact-hexagonal distribution, as depicted in Fig. 3(a) and shown in Fig. 4(a). The space between the nanospheres is a key parameter for the next etching steps: if there is not enough space between consecutive structures, the fabrication will produce connected nanowires (see Supporting Information S1). To obtain a good separation of the nanowires, the diameter of polystyrene nanospheres was reduced

to approximately 550 nm (leaving about 450 nm space between them) using oxygen plasma in a reactive ion etching (RIE) system, see Fig. 3(b) and Fig. 4(b). This was performed in two steps to prevent a degradation of the sphere morphology the shrinking was made in two steps, using first a 5 min O_2 plasma at RF power = 20 W (and O_2 flow = 50 sccm, DC bias 250V, 0.070 mbar), followed by a second softer etching performed at 10 W RF power (and O_2 flow = 50 sccm, DC bias 160V, 0.070 mbar) for 8 min. It is important to note that the nanospheres cannot shrink more than half of their diameter, otherwise they lose their spherical morphology (see Supporting Information Fig. S3), which will affect the uniformity of the nanowire array.

Using the shrunk spheres as a mask, SiO_2 etching was performed using a RIE system with CHF_3 chemistry (RF power of 50 W, DC bias 390V, 15 sccm CHF_3 flow, 0.02 mbar pressure) for 25 min, see Fig. 3(c) and Supporting Information Fig. S4. After nanosphere removal in an ultrasonic methanol bath, the GaN sample was dry etched in an inductively coupled plasma (ICP) RIE system using CL_2-BCl_3 chemistry (30 W radio-frequency power, 100 W ICP power, 10 mTorr pressure, 10 sccm Cl_2 flow, 30 sccm BCl_3 flow, at 20°C for 150 min), as depicted in Fig. 3(d) and shown in Fig. 4(c). The etching rate for the sample under study was around 17 nm/min, resulting in 2.6 μm-long GaN nanowires, see Fig. 3(d) and Fig. 4(c). The sidewall angle formed after the dry etching was $\theta = (6 \pm 1)°$, as illustrated in Fig. 3(d). Due to the sidewall angle obtained after dry etching, the maximum NW length ($L_{dry,max}$) is a function of the separation between consecutive spheres (t_{gap}) and given by $L_{max} = \frac{t_{gap}}{2\tan(\theta)}$. Thus, using the parameter described here, $t_{gap} = 450\ nm$, the maximum achievable length an array of well separated nanowire is around (2.1 ± 0.3) μm.

Finally, wet etching in AZ400K (KOH containing developer) was used to smooth the NW sidewalls, removing the damaged material and exposing the *m*-{10-10} planes,[43] as illustrated in Fig. 3(e) and shown in Fig. 4(c). Wet etching was performed at 65°C for 6-8 h, depending on the desired nanowire diameter, resulting in an ~ 60 nm/h etching rate of the nanowire sidewalls. The final nanowire length was 2.3 μm (see Supporting Information Fig. S5), with a dispersion in NW diameter between 60-200 nm, see Fig. 3(e). A total yield as good as 70% was observed. Etching of the top c-plane in Ga-polar GaN using KOH is expected, as previously reported[45,46]. Thus, a shortening of the nanowire length is expected after the wet etching, as depicted in Fig. 3(e). We have measured a roughly SiO_2 etching rate during the dry etching (~ 2 nm/min), which means that an approximately 300 nm SiO_2 remained after the step IV. This remained SiO_2 layer acted as a protective layer for the wet etching, at least in the beginning of the process, since it will be also etched at same point, as illustrated in Fig. 3(e). We have measured also the etching rate of the SiO_2 on the AZ400K at 65 °C, ~ 100 nm/h. Then, some etching of the top facet in the fabricated nanowires is expected.

The nanowires were mechanically detached from the sample and dispersed on a 40-nm-thick Si_3N_4 membrane chip by drop casting[23]. Single thin NWs (diameter below 100 nm) were electrically contacted by electron beam lithography and electron-beam evaporation of Ni/Au (150 nm/150 nm). In order to study the electric field created by the *p-i-n* junction, as well as the quality of the contacts on the fabricated NW devices, we performed EBIC measurements. In an EBIC experiment performed in a p-n junction, the electron-hole pairs created by the primary beam will be separated by the built-in electric field present in the depletion region, and the carriers will be collected in one of the two sides, generating an increase in the EBIC current only when its probing a region containing an internal field, mapping the presence of electric fields in the sample. In the absence of schottky induced fields, for a perfect p-n junction, a clear peak should be observed.[47,48] The collection side defines which carrier will be measured, electrons from the n-side (holes from the p-side); thus, inverting the collecting side, the same peak, with an inversion on the signal of EBIC current should be observed.

In Fig. 5(a) we can see the results of the EBIC performed in a single GaN NW. Collecting the current from the *p*-side, orange profile in Fig. 5(a), the presence of an internal field is clearly observed as a positive current peak close to the left contact in Fig. 5(a). We can also see that the contact at the *p*-side is ohmic: no current peak related with a Schottky barrier is observed near the right contact on the *p*-type GaN. Inverting the current collection side, an inversion in the EBIC current is observed (see green EBIC signal in Fig. 5(a)), as expected in a *p-n* junction. Using Ni/Au to contact the n-side, and due to its high doping level, we expect the formation of a low resistance contact due to tunneling transport, however, because of the proximity with the field created by the *p-i-n* junction, the observation of a possible Schottky contact in the n-side is hindered. The unique and very localized EBIC peak at the

expected position (more than 1μm from the p-side, i.e. the top facet of the planar sample), and the inversion of the EBIC current when the collection side is changed, observed in Fig. 5(a), strongly suggest the presence of a built-in electric field created by the *p-i-n* junction. In addition, it demonstrates that the nanowire is not entirely depleted. In the case of a fully depleted NW it is expected that the EBIC signal extends over the entire NW length, as previously observed[14].

The relation between the depletion region width (W_d) and the surface band bending ($\emptyset_{sbb}$) is given by $\sqrt{4\varepsilon_0\varepsilon_s\emptyset_{sbb}/q^2N_{A,D}}$ where $\varepsilon_s = 9.5$ is the dielectric constant of GaN, $\varepsilon_0 = 8.85 \times 10^{-14}\ C/Vcm$ is the vacuum permeability, $q = 1.6 \times 10^{-19}\ C$ is the elementary charge and $N_{A,D}$ is the dopant density of the *p* or *n* regions. Assuming a band bending of 1.4 eV for the p-side [49] and 0.6 eV for the n-side [50,51] at the doping level measured by SIMS measurements($[Mg] = 3.9 \times 10^{19}\ cm^{-3}$; $[\mathrm{Si}] = 4.9 \times 10^{18}\ cm^{-3}$), the depletion region length at the surface of the *p*-type and *n*-type sides of the nanowire would be around $W_{d,p\ region} \cong 9\ nm$ and $W_{d,n\ region} \cong 16\ nm$, respectively, much smaller than the diameter, around 75 nm (aspect ratio 31). However, the short intermediate undoped region is expected to be fully depleted, as schematically shown in Fig. 5(b).

Fig. 5(c) shows the I−V characteristics of the same NW depicted in Fig. 5(a), recorded in the dark and under illumination at 325 nm, applying bias to the *p*-side of the nanowire with the *n*-side connected to ground. The device displays the expected rectifying behavior, with an increase of the current under UV illumination. The variation of the photocurrent (I_{ph}) as a function of the incident optical power (P) was studied under bias in the range of +2V to -2V, with the result presented in Fig. 6. The photocurrent scales linearly with the optical power for all the values of bias under study, both forward and reverse bias. This trend is consistent with the trend observed in planar GaN *p-i-n* photodiodes[52], but it is unusual in single-NW photodetectors. Linear single-NW photodetectors have been demonstrated only under reverse bias, these detectors become non-linear under forward bias[14,15]. Under increasing reverse bias (forward bias), a broadening (narrowing) of the *p-i-n* junction depletion region is expected and, consequently, more (less) photogenerated electron-hole pairs are collected, increasing (decreasing) the photocurrent. The linearity observed here at +2 V bias (Fig. 6) implies that there is still a depletion region in the intrinsic segment, allowing the drift collection of photogenerated electron-hole pairs.

Previous UV photodetectors based on GaN nanowires containing a p-n junction[14] or not[13,15] presented sublinear photoresponse for nanowires with a large diameter. In general, non-core-shell GaN single-NW photodetectors present a sublinear photoresponse with excitation power due to the modulation of the surface band bending under illumination.[15] As a result of Fermi level pinning at the nanowire sidewalls, surface band bending occurs, and the region near to the nanowire surface is depleted, however, mobile charges are still present in the nanowire core, for larger diameter nanowires. Ultraviolet illumination is known to unpin the Fermi level at the nanowire sidewalls.[53] The photocurrent will be mainly generated in the conductive nanowire core. Thus, the variation of the surface band bending upon UV illumination will modify the region where photons are collected in a nonlinear way, for the larger diameter NWs, leading to the sublinear photoresponse. It is interesting that the sublinear photoresponse can be avoided by making NWs with a small diameter. In this case, they are totally depleted, and the light-induced change in the Fermi level at the sidewalls will not be the dominant phenomenon, making the photoresponse linear.[15]

Here, the linearity of the photocurrent is attributed to the presence of a *p-i-n* structure. The photodetection occurs mainly in the intrinsic region due to the presence of the electric field generated by the *p* and *n* regions. The intrinsic region is totally depleted, due to the small diameter of the nanowire under study. Thus, the presence of the intrinsic region guarantees the linear photoresponse. Also, in the NW under study, the *p* and *n* regions are not fully depleted, which means that the diode has a series resistance that is sensitive to surface states. However, the linear photoresponse observed here implies that the photocurrent is dominated by carrier drift in the depletion region, whose effect is dominant with respect to the NW surface. The fact that, even under forward bias (in our work +2V), the detector behaves linearly, indicates that we still have a depletion region in the intrinsic section, different from a simple *p-n* junction nanowire.[14]. Therefore, in contrast to previous works, our results show that it is possible to fabricate linear UV photodetectors over a wider applied bias range based on GaN nanowires by exploiting an axial *p-i-n* structure and a small diameter at the same time, leading to an axial built-in electric field induced by the *p-i-n* junction being dominant over surface effects. In addition, a *p-i-n* structure is interesting because the partially depleted *n* and *p*-segments, in principle, would allow the

detection of higher electrical currents (if better ohmic contacts are made), which is not the case in a linear single-NW photodetector that is entirely depleted.

4 Conclusions

In summary, we have developed a process to fabricate top-down GaN nanowires combining nanosphere lithography, CHF_3-based ICP-RIE and KOH-based crystallographic-selective wet etching. Long (> 2 µm) NWs with diameters below 200 nm with smooth sidewalls and aspect ratios above 30 were obtained from a planar sample containing a *p-i-n* structure. The formation of the *p-i-n* junction was investigated by SIMS and STEM-DPC on the as grown sample and a FIB lamella tailored from the as-grown sample. Moreover, the *p-i-n* junction was studied by EBIC, IV and power dependent photocurrent measurements. A dopant concentration of $N_D = 4.9 \times 10^{18}\ cm^{-3}$ and $N_A = 3.9 \times 10^{19}\ cm^{-3}$ was revealed by SIMS, with a 50 nm depletion width at zero-bias measured by DPC, as expected from the growth conditions. The top-down fabrication process did not affect the electrical behavior of the *p-i-n* junction, as confirmed by EBIC and current-voltage measurements. The investigation of the performance of the top-down NWs as single-NW photodetectors showed a linear response as a function of the UV excitation power, which implies that the photoresponse is dominated by carrier drift in the depletion region, whose effect is dominant with respect to the NW surface effects. As an outlook, it would be interesting to study the electro-optical variability between as fabricated single nanowire photodetectors, to assess the influence of small diameter variations as well as the potential influence of crystal defects. Moreover, it would be interesting to measure the internal electric field more quantitatively both inside the nanowire as well as in the FIB lamella, similar to the studies shown for more traditional semiconductors [54]. Finally, these studies will also show optimal NW fabrication conditions allowing reliable fabrication of planarized nanowire array photodetectors.

Corresponding authors

bruno-cesar.da-silva@neel.cnrs.fr, martien.den-hertog@neel.cnrs.fr

Supporting Information

The Supporting Information is available free of charge at https://pubs.acs.org/doi/10.1021/acsanm.3c01495.

- Additional SEM images of the NW fabrication process using nanosphere lithography (PDF)

Acknowledgement

This project received funding from the European Research Council under the European Union's H2020 Research and Innovation programme via the e-See project (Grant No. 758385). This work was also partially funded by the Program Initiatives de Recherche Stratégiques (IRS) of IDEX Université Grenoble Alpes (ANR-15-IDEX-0002) and by the French National Research Agency in the framework of the HARAIN program ANR-22-CE51-0032. A CC-BY public copyright license has been applied by the authors to the present document and will be applied to all subsequent versions up to the Author Accepted Manuscript arising from this submission, in accordance with the grant's open access conditions. These experiments have been performed at the Nanocharacterisation platform PFNC in Minatec, Grenoble.

Data Availability Statement

The data that support the findings of this study are available from the corresponding authors upon reasonable request.

Notes

The authors declare no competing financial interest.

References

(1) Cai, Q.; You, H.; Guo, H.; Wang, J.; Liu, B.; Xie, Z.; Chen, D.; Lu, H.; Zheng, Y.; Zhang, R. Progress on AlGaN-Based Solar-Blind Ultraviolet Photodetectors and Focal Plane Arrays. *Light Sci Appl* **2021**, *10* (1), 94. https://doi.org/10.1038/s41377-021-00527-4.
(2) Peng, L.; Hu, L.; Fang, X. Low-Dimensional Nanostructure Ultraviolet Photodetectors. *Adv. Mater.* **2013**, *25* (37), 5321–5328. https://doi.org/10.1002/adma.201301802.
(3) Chen, H.; Liu, K.; Hu, L.; Al-Ghamdi, A. A.; Fang, X. New Concept Ultraviolet Photodetectors. *Materials Today* **2015**, *18* (9), 493–502. https://doi.org/10.1016/j.mattod.2015.06.001.
(4) Sang, L.; Liao, M.; Sumiya, M. A Comprehensive Review of Semiconductor Ultraviolet Photodetectors: From Thin Film to One-Dimensional Nanostructures. *Sensors* **2013**, *13* (8), 10482–10518. https://doi.org/10.3390/s130810482.
(5) Monroy, E.; Muñoz, E.; Sánchez, F. J.; Calle, F.; Calleja, E.; Beaumont, B.; Gibart, P.; Muñoz, J. A.; Cussó, F. High-Performance GaN p-n Junction Photodetectors for Solar Ultraviolet Applications. *Semicond. Sci. Technol.* **1998**, *13* (9), 1042–1046. https://doi.org/10.1088/0268-1242/13/9/013.
(6) Zhang, Y.; Shen, S.-C.; Kim, H. J.; Choi, S.; Ryou, J.-H.; Dupuis, R. D.; Narayan, B. Low-Noise GaN Ultraviolet p-i-n Photodiodes on GaN Substrates. *Appl. Phys. Lett.* **2009**, *94* (22), 221109. https://doi.org/10.1063/1.3148812.
(7) Ji, M.-H.; Kim, J.; Detchprohm, T.; Dupuis, R. D.; Sood, A. K.; Dhar, N. K.; Lewis, J. Uniform and Reliable GaN P-i-n Ultraviolet Avalanche Photodiode Arrays. *IEEE Photon. Technol. Lett.* **2016**, *28* (19), 2015–2018. https://doi.org/10.1109/LPT.2016.2580038.
(8) Ji, D.; Ercan, B.; Benson, G.; Newaz, A. K. M.; Chowdhury, S. 60 A/W High Voltage GaN Avalanche Photodiode Demonstrating Robust Avalanche and High Gain up to 525 K. *Appl. Phys. Lett.* **2020**, *116* (21), 211102. https://doi.org/10.1063/1.5140005.
(9) Kind, H.; Yan, H.; Messer, B.; Law, M.; Yang, P. Nanowire Ultraviolet Photodetectors and Optical Switches. *Advanced Materials* **2002**, *14* (2), 158–160. https://doi.org/10.1002/1521-4095(20020116)14:2<158::AID-ADMA158>3.0.CO;2-W.
(10) Soci, C.; Zhang, A.; Bao, X.-Y.; Kim, H.; Lo, Y.; Wang, D. Nanowire Photodetectors. *j nanosci nanotechnol* **2010**, *10* (3), 1430–1449. https://doi.org/10.1166/jnn.2010.2157.
(11) LaPierre, R. R.; Robson, M.; Azizur-Rahman, K. M.; Kuyanov, P. A Review of III–V Nanowire Infrared Photodetectors and Sensors. *Journal of Physics D: Applied Physics* **2017**, *50* (12), 123001. https://doi.org/10.1088/1361-6463/aa5ab3.
(12) Spies, M.; Monroy, E. Nanowire Photodetectors Based on Wurtzite Semiconductor Heterostructures. *Semicond. Sci. Technol.* **2019**, *34* (5), 053002. https://doi.org/10.1088/1361-6641/ab0cb8.
(13) González-Posada, F.; Songmuang, R.; Den Hertog, M.; Monroy, E. Room-Temperature Photodetection Dynamics of Single GaN Nanowires. *Nano Lett.* **2012**, *12* (1), 172–176. https://doi.org/10.1021/nl2032684.
(14) Cuesta, S.; Spies, M.; Boureau, V.; Donatini, F.; Hocevar, M.; den Hertog, M. I.; Monroy, E. Effect of Bias on the Response of GaN Axial p–n Junction Single-Nanowire Photodetectors. *Nano Lett.* **2019**, *19* (8), 5506–5514. https://doi.org/10.1021/acs.nanolett.9b02040.
(15) Spies, M.; Polaczyński, J.; Ajay, A.; Kalita, D.; Luong, M. A.; Lähnemann, J.; Gayral, B.; den Hertog, M. I.; Monroy, E. Effect of the Nanowire Diameter on the Linearity of the Response of GaN-Based Heterostructured Nanowire Photodetectors. *Nanotechnology* **2018**, *29* (25), 255204. https://doi.org/10.1088/1361-6528/aab838.
(16) Bertness, K. A.; Sanford, N. A.; Davydov, A. V. GaN Nanowires Grown by Molecular Beam Epitaxy. *IEEE J. Select. Topics Quantum Electron.* **2011**, *17* (4), 847–858. https://doi.org/10.1109/JSTQE.2010.2082504.
(17) Knelangen, M.; Consonni, V.; Trampert, A.; Riechert, H. *In Situ* Analysis of Strain Relaxation during Catalyst-Free Nucleation and Growth of GaN Nanowires. *Nanotechnology* **2010**, *21* (24), 245705. https://doi.org/10.1088/0957-4484/21/24/245705.
(18) Landré, O.; Bougerol, C.; Renevier, H.; Daudin, B. Nucleation Mechanism of GaN Nanowires Grown on (111) Si by Molecular Beam Epitaxy. *Nanotechnology* **2009**, *20* (41), 415602. https://doi.org/10.1088/0957-4484/20/41/415602.

(19) Kim, W.; Güniat, L.; Fontcuberta i Morral, A.; Piazza, V. Doping Challenges and Pathways to Industrial Scalability of III–V Nanowire Arrays. *Applied Physics Reviews* **2021**, *8* (1), 011304. https://doi.org/10.1063/5.0031549.
(20) Grossklaus, K. A.; Banerjee, A.; Jahangir, S.; Bhattacharya, P.; Millunchick, J. M. Misorientation Defects in Coalesced Self-Catalyzed GaN Nanowires. *Journal of Crystal Growth* **2013**, *371*, 142–147. https://doi.org/10.1016/j.jcrysgro.2013.02.019.
(21) Brandt, O.; Fernández-Garrido, S.; Zettler, J. K.; Luna, E.; Jahn, U.; Chèze, C.; Kaganer, V. M. Statistical Analysis of the Shape of One-Dimensional Nanostructures: Determining the Coalescence Degree of Spontaneously Formed GaN Nanowires. *Crystal Growth & Design* **2014**, *14* (5), 2246–2253. https://doi.org/10.1021/cg401838q.
(22) Gomes, U. P.; Ercolani, D.; Zannier, V.; Beltram, F.; Sorba, L. Controlling the Diameter Distribution and Density of InAs Nanowires Grown by Au-Assisted Methods. *Semicond. Sci. Technol.* **2015**, *30* (11), 115012. https://doi.org/10.1088/0268-1242/30/11/115012.
(23) Spies, M.; Sadre Momtaz, Z.; Lähnemann, J.; Anh Luong, M.; Fernandez, B.; Fournier, T.; Monroy, E.; I den Hertog, M. Correlated and In-Situ Electrical Transmission Electron Microscopy Studies and Related Membrane-Chip Fabrication. *Nanotechnology* **2020**, *31* (47), 472001. https://doi.org/10.1088/1361-6528/ab99f0.
(24) Melanson, B.; Hartensveld, M.; Liu, C.; Zhang, J. Realization of Electrically Driven AlGaN Micropillar Array Deep-Ultraviolet Light Emitting Diodes at 286 Nm. *AIP Advances* **2021**, *11* (9), 095005. https://doi.org/10.1063/5.0061381.
(25) Hartensveld, M.; Melanson, B.; Liu, C.; Zhang, J. AlGaN Nanowires with Inverse Taper for Flexible DUV Emitters. *J. Phys. Photonics* **2021**, *3* (2), 024016. https://doi.org/10.1088/2515-7647/abf6be.
(26) Olivier, F.; Tirano, S.; Dupré, L.; Aventurier, B.; Largeron, C.; Templier, F. Influence of Size-Reduction on the Performances of GaN-Based Micro-LEDs for Display Application. *Journal of Luminescence* **2017**, *191*, 112–116. https://doi.org/10.1016/j.jlumin.2016.09.052.
(27) Cheung, C. L.; Nikolić, R. J.; Reinhardt, C. E.; Wang, T. F. Fabrication of Nanopillars by Nanosphere Lithography. *Nanotechnology* **2006**, *17* (5), 1339–1343. https://doi.org/10.1088/0957-4484/17/5/028.
(28) Kim, B.-J.; Jung, H.; Kim, H.-Y.; Bang, J.; Kim, J. Fabrication of GaN Nanorods by Inductively Coupled Plasma Etching via SiO2 Nanosphere Lithography. *Thin Solid Films* **2009**, *517* (14), 3859–3861. https://doi.org/10.1016/j.tsf.2009.01.144.
(29) Li, Q.; Westlake, K. R.; Crawford, M. H.; Lee, S. R.; Koleske, D. D.; Figiel, J. J.; Cross, K. C.; Fathololoumi, S.; Mi, Z.; Wang, G. T. Optical Performance of Top-down Fabricated InGaN/GaN Nanorod Light Emitting Diode Arrays. *Opt. Express* **2011**, *19* (25), 25528. https://doi.org/10.1364/OE.19.025528.
(30) Won Woo Chung; Gang Yeol Yoo; Park, H. K.; Kim, W.; Young Rag Do. Fabrication of an InGaN/GaN-Based LED Nanorod Array by Nanosphere Lithography and Its Optical Properties. In *2015 IEEE 15th International Conference on Nanotechnology (IEEE-NANO)*; IEEE: Rome, 2015; pp 216–219. https://doi.org/10.1109/NANO.2015.7388961.
(31) Granz, T.; Mariana, S.; Hamdana, G.; Yu, F.; Fatahilah, M. F.; Clavero, I. M.; Puranto, P.; Li, Z.; Brand, U.; Prades, J. D.; Peiner, E.; Waag, A.; Wasisto, H. S. Nanofabrication of Vertically Aligned 3D GaN Nanowire Arrays with Sub-50 Nm Feature Sizes Using Nanosphere Lift-off Lithography. In *Proceedings of Eurosensors 2017, Paris, France, 3–6 September 2017*; MDPI, 2017; p 309. https://doi.org/10.3390/proceedings1040309.
(32) Mariana, S.; Gülink, J.; Hamdana, G.; Yu, F.; Strempel, K.; Spende, H.; Yulianto, N.; Granz, T.; Prades, J. D.; Peiner, E.; Wasisto, H. S.; Waag, A. Vertical GaN Nanowires and Nanoscale Light-Emitting-Diode Arrays for Lighting and Sensing Applications. *ACS Appl. Nano Mater.* **2019**, *2* (7), 4133–4142. https://doi.org/10.1021/acsanm.9b00587.
(33) Zou, X.; Zhang, X.; Zhang, Y.; Lyu, Q.; Tang, C. W.; Lau, K. M. GaN Single Nanowire p–i–n Diode for High-Temperature Operations. *ACS Appl. Electron. Mater.* **2020**, *2* (3), 719–724. https://doi.org/10.1021/acsaelm.9b00801.
(34) Zhang, H.; Dai, X.; Guan, N.; Messanvi, A.; Neplokh, V.; Piazza, V.; Vallo, M.; Bougerol, C.; Julien, F. H.; Babichev, A.; Cavassilas, N.; Bescond, M.; Michelini, F.; Foldyna, M.; Gautier, E.; Durand, C.; Eymery, J.; Tchernycheva, M. Flexible Photodiodes Based on Nitride Core/Shell p–n

Junction Nanowires. *ACS Appl. Mater. Interfaces* **2016**, *8* (39), 26198–26206. https://doi.org/10.1021/acsami.6b06414.
(35) Gogneau, N.; Chrétien, P.; Sodhi, T.; Couraud, L.; Leroy, L.; Travers, L.; Harmand, J.-C.; Julien, F. H.; Tchernycheva, M.; Houzé, F. Electromechanical Conversion Efficiency of GaN NWs: Critical Influence of the NW Stiffness, the Schottky Nano-Contact and the Surface Charge Effects. *Nanoscale* **2022**, *14* (13), 4965–4976. https://doi.org/10.1039/D1NR07863A.
(36) Krogstrup, P.; Jørgensen, H. I.; Heiss, M.; Demichel, O.; Holm, J. V.; Aagesen, M.; Nygard, J.; Fontcuberta i Morral, A. Single-Nanowire Solar Cells beyond the Shockley–Queisser Limit. *Nature Photonics* **2013**, *7* (4), 306–310. https://doi.org/10.1038/nphoton.2013.32.
(37) Xu, Y.; Gong, T.; Munday, J. N. The Generalized Shockley-Queisser Limit for Nanostructured Solar Cells. *Scientific Reports* **2015**, *5*, 13536.
(38) Calarco, R.; Marso, M.; Richter, T.; Aykanat, A. I.; Meijers, R.; v.d. Hart, A.; Stoica, T.; Lüth, H. Size-Dependent Photoconductivity in MBE-Grown GaN−Nanowires. *Nano Lett.* **2005**, *5* (5), 981–984. https://doi.org/10.1021/nl0500306.
(39) Mukhtarova, A.; Valdueza-Felip, S.; Redaelli, L.; Durand, C.; Bougerol, C.; Monroy, E.; Eymery, J. Dependence of the Photovoltaic Performance of Pseudomorphic InGaN/GaN Multiple-Quantum-Well Solar Cells on the Active Region Thickness. *Appl. Phys. Lett.* **2016**, *108* (16), 161907. https://doi.org/10.1063/1.4947445.
(40) Mukhtarova, A.; Valdueza-Felip, S.; Durand, C.; Pan, Q.; Grenet, L.; Peyrade, D.; Bougerol, C.; Chikhaoui, W.; Monroy, E.; Eymery, J. InGaN/GaN Multiple-quantum Well Heterostructures for Solar Cells Grown by MOVPE: Case Studies. *Phys. Status Solidi C* **2013**, *10* (3), 350–354. https://doi.org/10.1002/pssc.201200682.
(41) Haas, B.; Rouvière, J.-L.; Boureau, V.; Berthier, R.; Cooper, D. Direct Comparison of Off-Axis Holography and Differential Phase Contrast for the Mapping of Electric Fields in Semiconductors by Transmission Electron Microscopy. *Ultramicroscopy* **2019**, *198*, 58–72. https://doi.org/10.1016/j.ultramic.2018.12.003.
(42) da Silva, B. C.; Momtaz, Z. S.; Bruas, L.; Rouviere, J.-L.; Okuno, H.; Cooper, D.; den-Hertog, M. I. The Influence of Illumination Conditions in the Measurement of Built-in Electric Field at p–n Junctions by 4D-STEM. *Applied Physics Letters* **2022**, *121* (12), 123503. https://doi.org/DOI: 10.1063/5.0104861.
(43) Cuesta, S.; Denaix, L.; Castioni, F.; Dang, L. S.; Monroy, E. Reduction of the Lasing Threshold in Optically Pumped AlGaN/GaN Lasers with Two-Step Etched Facets. *Semicond. Sci. Technol.* **2022**, *37* (7), 075013. https://doi.org/10.1088/1361-6641/ac7164.
(44) Liu, J.; Chen, C.; Yang, G.; Chen, Y.; Yang, C.-F. Effect of the Fabrication Parameters of the Nanosphere Lithography Method on the Properties of the Deposited Au-Ag Nanoparticle Arrays. *Materials* **2017**, *10* (4), 381. https://doi.org/10.3390/ma10040381.
(45) Oliva, M.; Kaganer, V.; Pudelski, M.; Meister, S.; Tahraoui, A.; Geelhaar, L.; Brandt, O.; Auzelle, T. A Route for the Top-down Fabrication of Ordered Ultrathin GaN Nanowires. *Nanotechnology* **2023**, *34* (20), 205301. https://doi.org/10.1088/1361-6528/acb949.
(46) Li, D.; Sumiya, M.; Yoshimura, K.; Suzuki, Y.; Fukuda, Y.; Fuke, S. Characteristics of the GaN Polar Surface during an Etching Process in KOH Solution. *phys. stat. sol. (a)* **2000**, *180* (1), 357–362. https://doi.org/10.1002/1521-396X(200007)180:1<357::AID-PSSA357>3.0.CO;2-F.
(47) Conlan, A. P.; Moldovan, G.; Bruas, L.; Monroy, E.; Cooper, D. Electron Beam Induced Current Microscopy of Silicon *p–n* Junctions in a Scanning Transmission Electron Microscope. *Journal of Applied Physics* **2021**, *129* (13), 135701. https://doi.org/10.1063/5.0040243.
(48) Tchoulfian, P.; Donatini, F.; Levy, F.; Dussaigne, A.; Ferret, P.; Pernot, J. Direct Imaging of p–n Junction in Core–Shell GaN Wires. *Nano Lett.* **2014**, *14* (6), 3491–3498. https://doi.org/10.1021/nl5010493.
(49) Hashizume, T. Effects of Mg Accumulation on Chemical and Electronic Properties of Mg-Doped *p* -Type GaN Surface. *Journal of Applied Physics* **2003**, *94* (1), 431–436. https://doi.org/10.1063/1.1580195.
(50) Van de Walle, C. G.; Segev, D. Microscopic Origins of Surface States on Nitride Surfaces. *Journal of Applied Physics* **2007**, *101* (8), 081704. https://doi.org/10.1063/1.2722731.
(51) Lymperakis, L.; Weidlich, P. H.; Eisele, H.; Schnedler, M.; Nys, J.-P.; Grandidier, B.; Stiévenard, D.; Dunin-Borkowski, R. E.; Neugebauer, J.; Ebert, Ph. Hidden Surface States at Non-Polar GaN

(101¯0) Facets: Intrinsic Pinning of Nanowires. *Appl. Phys. Lett.* **2013**, *103* (15), 152101. https://doi.org/10.1063/1.4823723.
(52) Monroy, E.; Omnès, F.; Calle, F. Wide-Bandgap Semiconductor Ultraviolet Photodetectors. *Semicond. Sci. Technol.* **2003**, *18* (4), R33–R51. https://doi.org/10.1088/0268-1242/18/4/201.
(53) Pfüller, C.; Brandt, O.; Grosse, F.; Flissikowski, T.; Chèze, C.; Consonni, V.; Geelhaar, L.; Grahn, H. T.; Riechert, H. Unpinning the Fermi Level of GaN Nanowires by Ultraviolet Radiation. *Phys. Rev. B* **2010**, *82* (4), 045320. https://doi.org/10.1103/PhysRevB.82.045320.
(54) da Silva, B. C.; Sadre Momtaz, Z.; Monroy, E.; Okuno, H.; Rouviere, J.-L.; Cooper, D.; Den Hertog, M. I. Assessment of Active Dopants and p–n Junction Abruptness Using In Situ Biased 4D-STEM. *Nano Lett.* **2022**, *22* (23), 9544–9550. https://doi.org/10.1021/acs.nanolett.2c03684.

FIGURE CAPTIONS

Figure 1 - (a) Schematic of the sample under study, a planar GaN *p-i-n* junction specimen grown by MOCVD. (b) SIMS of the sample shown in (a), indicating the dopant concentration in the bulk regions as $n = 4.9 \times 10^{18}\ cm^{-3}$ and $p = 3.9 \times 10^{19}\ cm^{-3}$.

Figure 2 - (a) Modulus of DPC-STEM image reflecting the strength of the electric field present in the 350 nm thick GaN lamella prepared from the sample shown in Figure 1. The DPC signal is proportional to the deflection of the electron beam, caused by the internal fields present in the sample. It is measured by taking the difference of incident electron intensity on two opposing quadrants of the DPC detector. A clear signal due to the presence of a built-in electric field created by the *p-i-n* is observed at the expected position (1.9 μm below the top surface). Some artifacts are still present due to the strong dynamical diffraction in the GaN, in spite of the off-axis orientation. (b) High Angle Annular Dark Field (HAADF) STEM image of the lamella prepared by FIB of the sample shown in (a). (c) Beam deflection profile averaged over the entire DPC map shown in (a) taken across the *p-i-n* junction: a depletion region width of 50 nm is measured, in agreement with the expected intermediate intrinsic region.

Figure 3 - Schematic of the optimized fabrication protocol to obtain the top-down GaN *p-i-n* junction nanowires: (a) Step I: Dispersion of 1 μm polystyrene nanospheres. (b) Step II: Shrinking of the spheres using a RIE oxygen plasma. (c) Step III: Etching of SiO_2 using RIE with CHF_3 chemistry. (d) Step IV: Dry etching of GaN performed in an ICP-RIE using BCL_3-Cl_2 chemistry. (e) Step V: Wet etching using AZ400K developer. As indicated in (c), due to the sidewall angle obtained after dry etching, the maximum NW length ($L_{dry,max}$) is a function of the separation between consecutive spheres (t_{gap}). The final NW length (L_{final}) will be slightly shorter than $L_{dry,max}$, due to the etch of the top GaN facet, once the remaining SiO_2 layer is removed.

Figure 4 - SEM images of some of the GaN nanowire fabrication steps described in Figure 3. (a) step I. (b) step II. (c) step IV. (d) step V.

Figure 5 - (a) EBIC scan along a single nanowire overlaid on an SEM image of the nanowire under study to illustrate where the scan was performed. The orange and green EBIC line scans correspond to current collection from the *n*-side and the *p*-side of the NW, respectively. (b) Schematic showing that the nanowire under study is partially depleted in the *n* and *p*-channels, while the intrinsic region is fully depleted. (c) I-V characteristics of the same NW shown in (a), in the dark (blue) and under ultraviolet illumination at 325 nm (red).

Figure 6 - Photocurrent measurements of the GaN *p-i-n* NW shown in Figure 5 as a function of the impinging optical power at 325 nm, measured under forward and reverse bias. The red dashed line illustrates the photocurrent scaling linearly with the optical power.

548

549

550 **Figure 1**

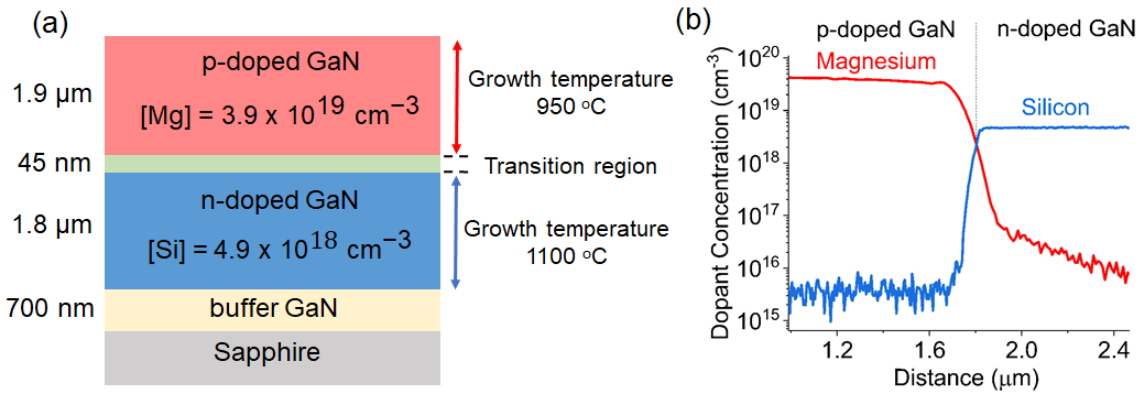

551

552

Figure 2

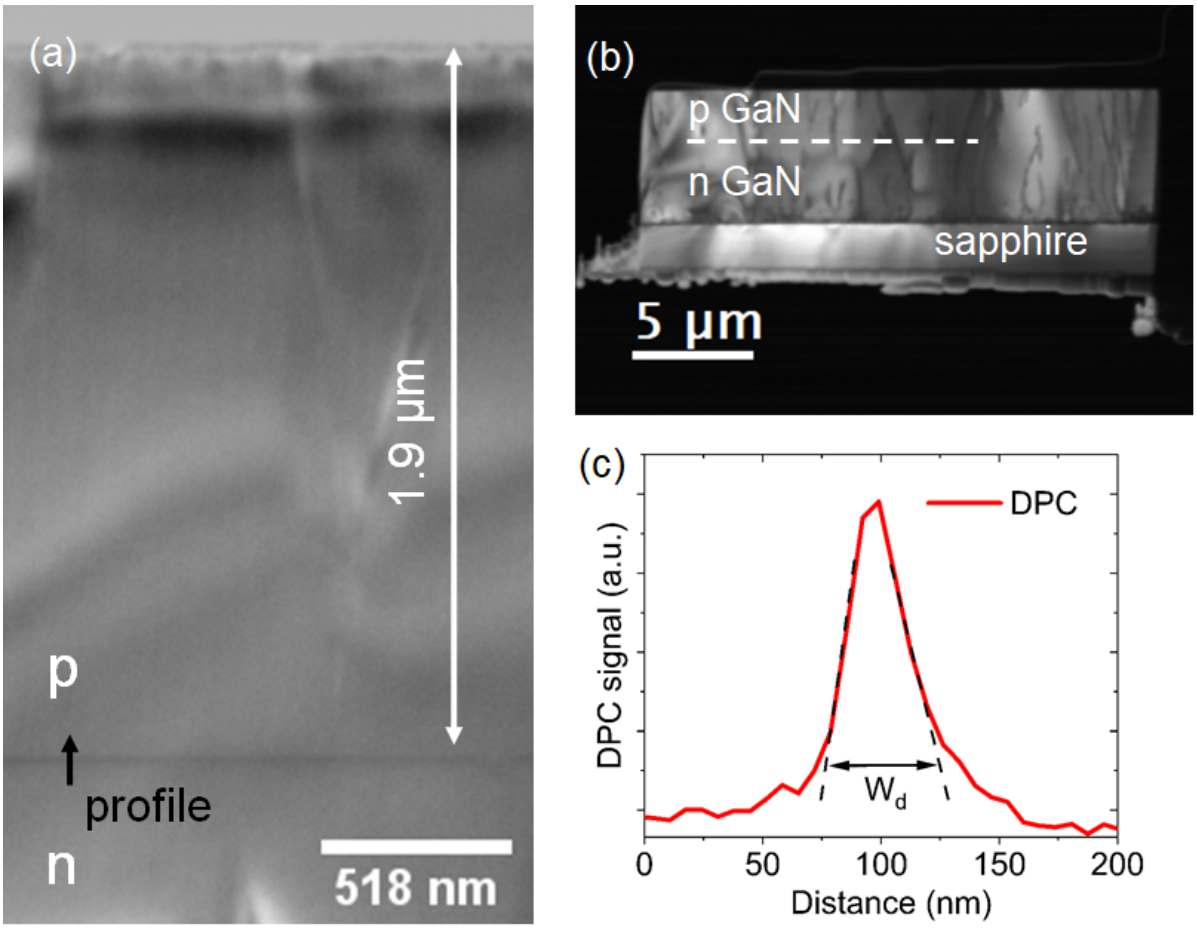
(a)
1.9 µm
p
profile
n
518 nm
(b)
p GaN
n GaN
sapphire
5 µm
(c)
DPC
DPC signal (a.u.)
W_d
0
50
100
150
200
Distance (nm)

Figure 3

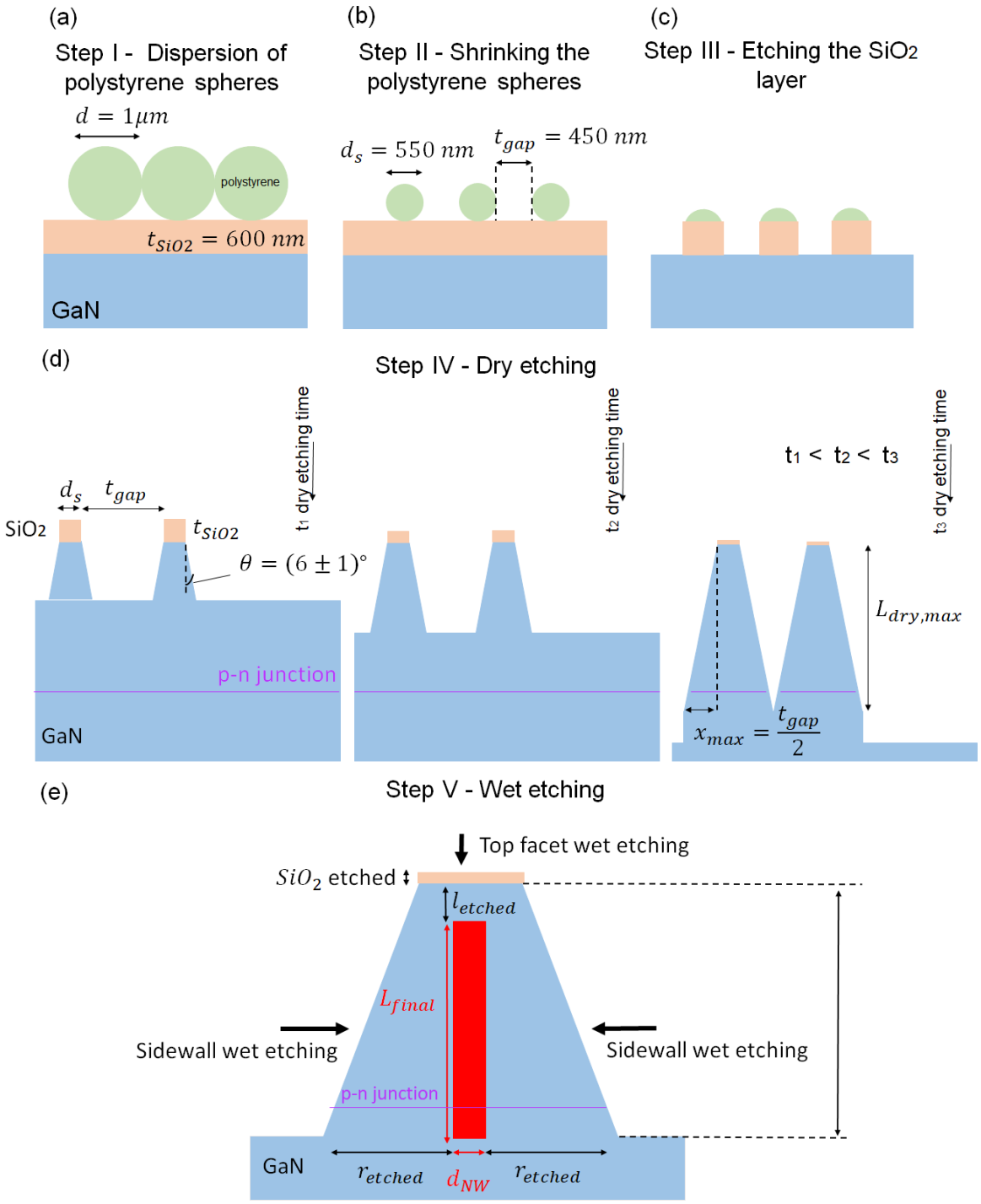
(a)
Step I - Dispersion of polystyrene spheres
$d = 1\mu m$
polystyrene
$t_{SiO2} = 600\ nm$
GaN
(b)
Step II - Shrinking the polystyrene spheres
$d_s = 550\ nm$
$t_{gap} = 450\ nm$
(c)
Step III - Etching the SiO2 layer
(d)
Step IV - Dry etching
t_1 dry etching time
t_2 dry etching time
t_3 dry etching time
$t_1 < t_2 < t_3$
d_s
t_{gap}
SiO2
t_{SiO2}
$\theta = (6 \pm 1)°$
p-n junction
GaN
$L_{dry,max}$
$x_{max} = \frac{t_{gap}}{2}$
(e)
Step V - Wet etching
Top facet wet etching
SiO_2 etched
l_{etched}
L_{final}
Sidewall wet etching
Sidewall wet etching
p-n junction
GaN
r_{etched}
d_{NW}
r_{etched}

564 **Figure 4**

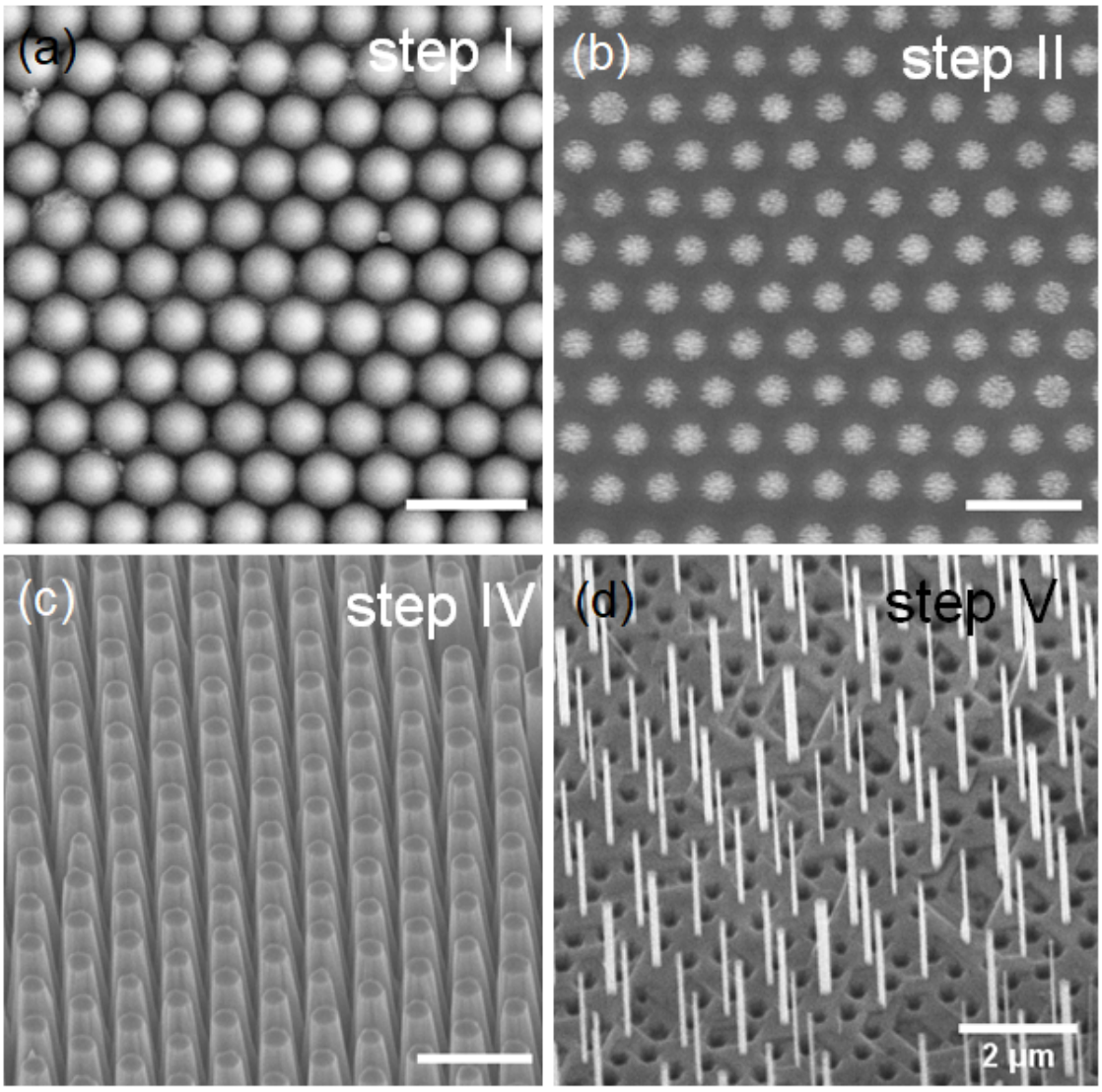

565

566

Figure 5

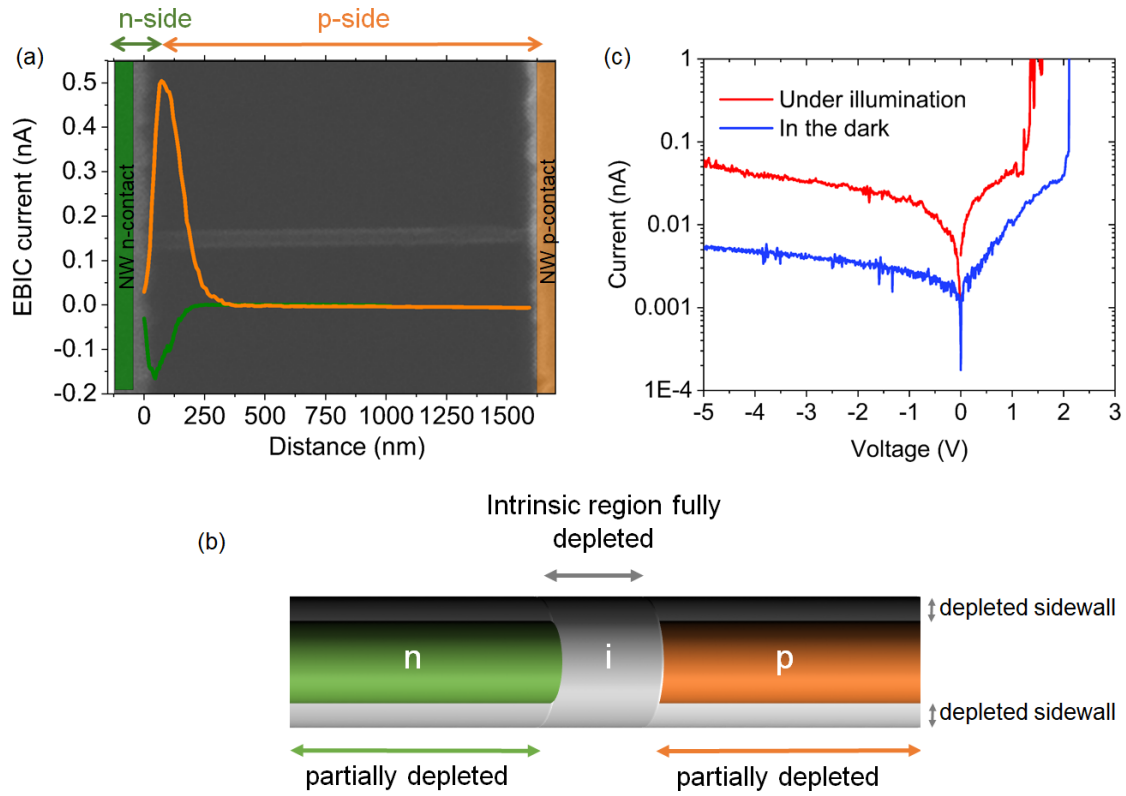
(a)
n-side
p-side
EBIC current (nA)
0.5
0.4
0.3
0.2
0.1
0.0
-0.1
-0.2
NW n-contact
NW p-contact
0
250
500
750
1000
1250
1500
Distance (nm)
(c)
1
0.1
0.01
0.001
1E-4
Current (nA)
Under illumination
In the dark
-5
-4
-3
-2
-1
0
1
2
3
Voltage (V)
(b)
Intrinsic region fully depleted
n
i
p
depleted sidewall
depleted sidewall
partially depleted
partially depleted

583 **Figure 6**

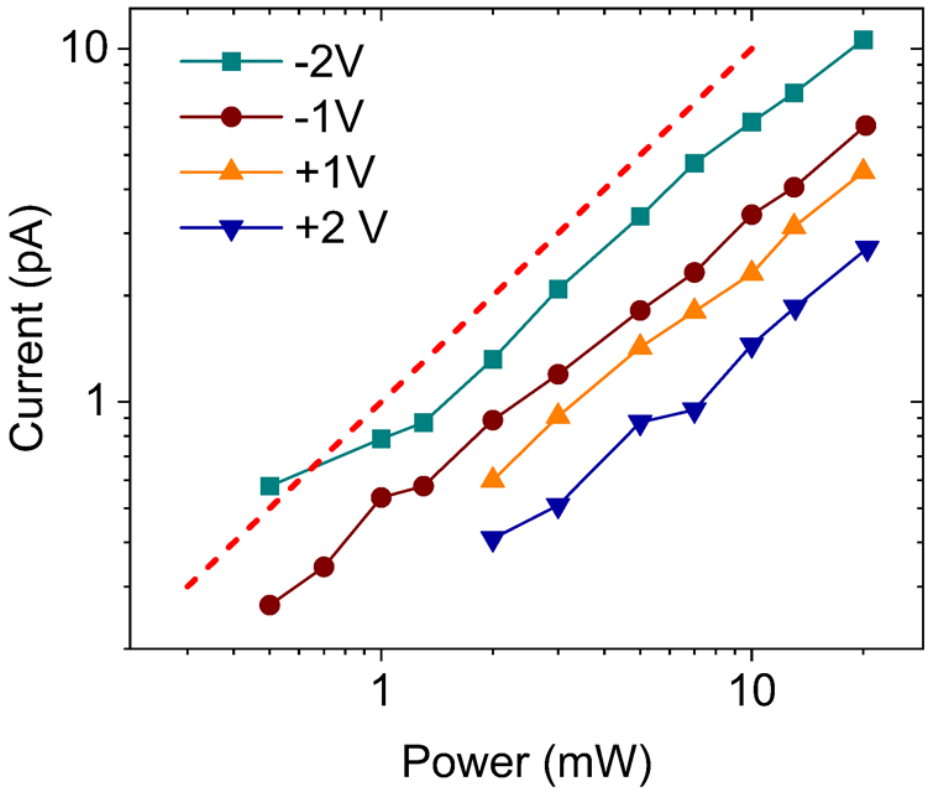

584

585

586 **TOC Figure**

587

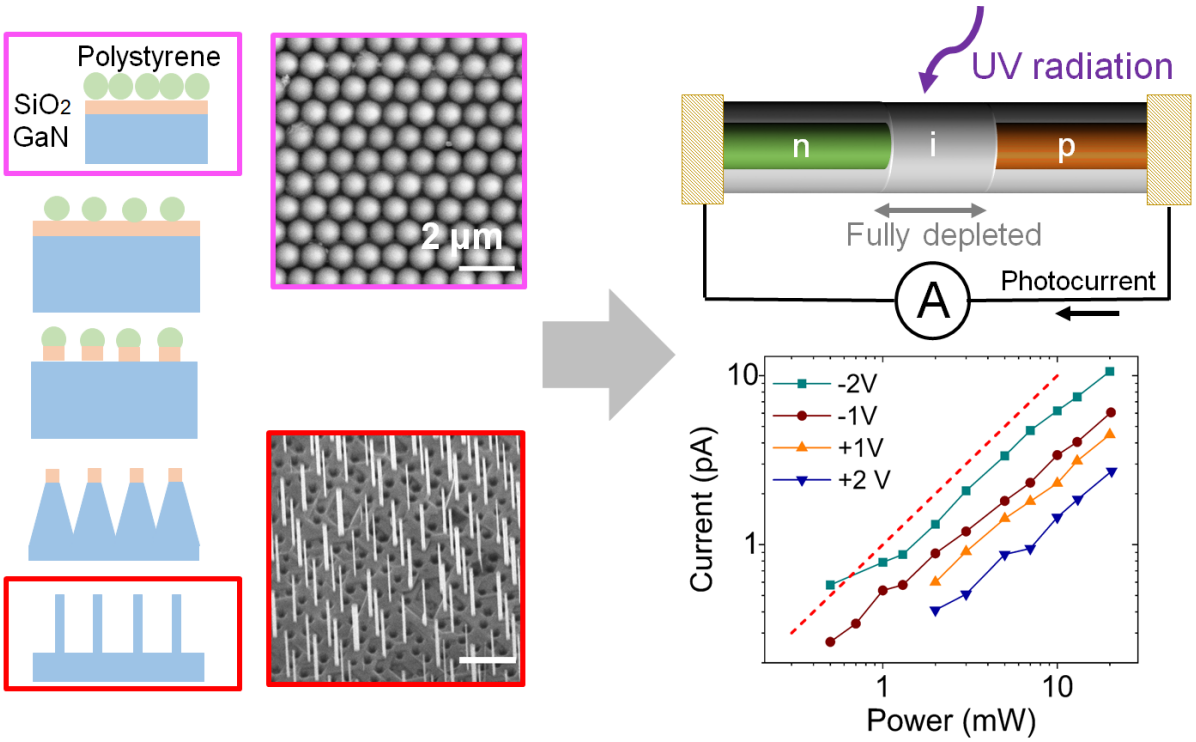

588

589

590

591